Lab on a Chip

PAPER

View Article Online
View Journal | View Issue

Check for updates

Cite this: *Lab Chip*, 2018, **18**, 3881

Received 1st August 2018,
Accepted 6th November 2018

DOI: 10.1039/c8lc00793d

rsc.li/loc

Mechanisms of multiphase reactive flow using biogenically calcite-functionalized micromodels

Wen Song,[a] Folake Ogunbanwo,[a] Marianne Steinsbø,[b] Martin A. Fernø[b] and Anthony R. Kovscek*[a]

Dissolution of carbonate minerals in porous media is important to many instances of subsurface flow, including geological carbon dioxide (CO_2) sequestration, karst formation, and crude-oil reservoir stimulation and acidizing. Of particular interest, geological CO_2 storage in deep carbonate reservoirs presents a significant long-term opportunity to mitigate atmospheric carbon emissions. The reactivity of carbonate reservoirs, however, may negatively impact storage formation integrity and hence jeopardize sequestered CO_2 storage security. In this work, we develop a novel biogenically calcite-functionalized microvisual device to study the fundamental pore-scale reactive transport dynamics in carbonate formations. Importantly, we discover a new microscale mechanism that dictates the overall behavior of the reactive transport phenomenon, where the reaction product, CO_2, due to carbonate rock dissolution forms a separate, protective phase that engulfs the carbonate rock grain and reduces further dissolution. The presence of the separate, protective CO_2 phase determines overall dissolution patterns in the storage reservoir and leads to formation of preferential leakage paths. We scale these results using nondimensional numbers to demonstrate their influence on industrial CO_2 storage security, safety, and capacity.

Introduction

Energy demand and climate tensions present some of the most pressing challenges facing the 21st century.[1,2] Global atmospheric CO_2 concentration increased from 270 ppm in 1750 (ref. 3) to 410 ppm in 2018 (ref. 4) due, in large part, to emissions from fossil fuel consumption.[5,6] Reducing atmospheric CO_2 emissions from fossil fuel combustion and other industrial sources is a key component in transitioning towards a low-carbon future.

Geological CO_2 storage in subsurface reservoirs provides an immediate industrial solution to limit large-scale CO_2 emissions and to transition to a low-carbon future.[7–9] Geological formations suitable for long-term carbon storage include deep saline aquifers, depleted oil and gas reservoirs, and unmineable coal seams.[10] Deep saline aquifers within carbonate formations, *i.e.*, limestones and dolostones, are ubiquitous and present the largest storage capacity worldwide.[11,12]

Carbonates, however, are extremely reactive and susceptible to dissolution in the presence of CO_2-acidified brines.[13,14] Storage reservoir rock dissolution undermines subsurface CO_2 storage security; uncertainty in injected CO_2 storage security currently forestalls large-scale implementation of subsurface CO_2 storage.[10,15,16] Predictive models describing reactive transport in geochemically complex carbonate reservoirs are thus required to design CO_2 injection schemes that maximize both storage capacity and storage security.

Predictive models assessing long-term geologic CO_2 storage potential require fundamental understanding of reservoir integrity[17,18] and CO_2 migration[19] based on fluid–rock interactions.[20,21] Core-scale reactive transport experiments provide pressure measurements, effluent analyses, and X-ray computed tomography that show significant reservoir rock dissolution due to CO_2-acidified brine.[22,23] Empirical relations derived from core-scale experiments have been developed to map the influence of acidity and advection on acid–rock reaction rates and dissolution patterns. Fredd and Fogler (1998) visualized uniform core-scale dissolution under high Damkohler number (Da) conditions and extended finger-like flow conduits under low Da conditions. The Damkohler number is defined as Da = reaction rate/advection rate. The reactions are represented by $2H^+_{(aq)} + CaCO_{3(s)} \rightarrow CO_2 + H_2O_{(l)} + Ca^{2+}_{(aq)}$.[23–26] Importantly, the current macroscopic core-scale literature does not assign a phase to the reaction product CO_2; all reaction products are assumed to be solubilized in the aqueous phase and reaction rates are assumed constant for prescribed acid fluxes.[23–26] Reactive transport models based on these assumptions require sample-specific

---

[a] *Department of Energy Resources Engineering, Stanford University, Stanford, CA 94305, USA. E-mail: kovscek@stanford.edu*

[b] *Department of Physics and Technology, University of Bergen, Bergen, Norway*

correction factors to match physical rock dissolution configurations.[21,24,25] New fundamental understanding of reactive transport mechanisms is therefore required to develop general predictive models for CO_2 storage.[27] More broadly, fundamental understanding of reactive transport in porous media applies to fields such as acidization of conventional petroleum reservoirs, shale reservoirs, and geothermal reservoirs, food processing,[28] and pharmaceutical manufacturing and uptake.

Pore-scale fluid–rock mechanisms ultimately dictate reactive transport in CO_2 storage reservoirs.[29] Specifically, pore-scale interfacial reaction dynamics determine macroscopic reaction rates and rock dissolution patterns.[30,31] Microfluidics provides direct real-time, pore-scale visualization of fluid transport and fluid–solid interactions through porous media.[13,32–41] Glass- and silicon-based microfluidic platforms with realistic pore geometries (micromodels) have been developed to enable pore-scale investigations under high-temperature, high-pressure geological conditions.[34–39,42–45] Pore-scale transport and reaction dynamics depend on mineralogy and rock surface chemistry. Mineral-functionalized pore surfaces enable direct visualization of the fundamental fluid–mineral interactions in microfluidic devices.[13,37,38,46]

In this study, we capture the physics describing pore-level reactive transport within carbonates in order to advance the understanding and design of secure geologic CO_2 storage. Novel carbonate-functionalized microfluidic devices are developed to study reactive transport at the interfacial, pore, and pore-ensemble scales using microfabrication and bacterial biogenesis. High-temperature, high-pressure, reactive transport experiments are scaled to replicate realistic CO_2 storage conditions. We find a new fundamental mechanism, grain engulfment, that dictates reactive transport and CO_2 storage security in carbonates through direct pore-scale visualization. Mechanistic understanding of fundamental interfacial dynamics is extended to determine practical implications within storage reservoirs through dimensionless analysis. The new, fundamental grain-engulfment mechanism impacts CO_2 storage security significantly close to injection wells in carbonate storage reservoirs.

Materials and methods

Pore-scale visualization of reactive transport through carbonates was achieved using calcite-functionalized microfluidics. Specifically, two types of calcite-functionalized flow devices were developed: (i) biogenically calcite-functionalized etched silicon micromodels that enable direct pore-scale visualization of reactive transport dynamics at elevated reservoir temperatures and pressures and (ii) crystalline calcite embedded polymer microchannels that enable direct quantitative studies of reactive transport under simpler hydrodynamic conditions. We define mineral-functionalized microfluidics as those with the mineralogy, morphology, and surface properties representative of the analogous real-rock system. That is, the calcite-functionalized micromodels developed here contain calcite grains in the pore space and are susceptible to reactive dissolution. The calcite-functionalized etched silicon micromodel provides a direct approach to visualize reactive transport dynamics under elevated temperature and pressure conditions typical of subsurface systems that was previously not attainable, and the calcite-embedded microchannel supplements the study by providing insight into the fundamental dynamics dictating reactive transport.

Biogenic calcite-functionalization of 2D porous medium

Current state-of-the-art etched silicon micromodels capture two-dimensional pore geometry accurately[34,37,38] to enable direct pore-scale visualization of fluid dynamics at elevated reservoir temperatures and pressures in rigid, non-reactive geological systems. Surface chemistry and reactive alteration of the pore structure, however, are not replicated. These properties underlie transport through carbonate porous media. The micromodels used in this work replicate pore geometries from thin-section images of real rock in order to capture realistic pore-geometry and pore-size distribution. Detailed design and fabrication methods are described by Buchgraber *et al.*[33,34,47] and are not the focus of this work. This section, instead, describes the novel method by which etched silicon micromodels are functionalized with calcite grains using bacteria.

Biogenic calcite-functionalization of the two-dimensional porous-media micromodels used the bacterium *Sporosarcina pasteurii*.[48] The bacterium *S. pasteurii* was chosen due to its well-documented ability to enable calcite precipitation and growth on solid surfaces.[48–52] That is, the calcite grains grown using this bacterial method are attached securely to the solid surfaces of the micromodel pore space. The bacteria were cultivated in brain heart infusion growth medium prior to delivery into the 2D silicon porous medium. The bacterial growth medium was prepared by mixing 47 g of brain heart infusion into 900 mL of deionized (DI) water. The well-mixed solution was sterilized for 15 minutes at 121 °C in an autoclave. The sterilized solution was cooled to ∼30 °C and a concentrated urea solution was added to make a 2 wt% urea broth. The urea solution was prepared by mixing 20 g of urea into 100 mL of DI water and was added to the broth by injecting the solution through a 0.2 μm filter. The bacteria were added to the growth medium to incubate to create the bacteria–broth injection solution.

The 2D silicon porous medium (micromodel) was initially saturated with DI water under atmospheric conditions to ensure an even deposition of bacteria. Microbial deposition within the pore spaces of the micromodel was achieved by injecting the bacteria-broth solution into the system. The bacteria-permeated micromodel was submerged in bacteria-free growth medium for 24 h to encourage *in situ* growth of the bacteria and to encourage adherence of the bacteria to the micromodel surface.

A cementation solution was injected into the bacteria-activated micromodel to induce calcite ($CaCO_{3(s)}$) precipitation. Specifically, the cementation solution was prepared by mixing 1 M urea (urea, U5378, Sigma) and 1 M calcium chloride (calcium chloride dehydrate, 31306, Sigma-Aldrich) in DI water. The cementation solution was injected into the bacteria-activated micromodel at a constant injection velocity of 10 m per day for 20 hours (Quizix QX pump). Calcite crystal growth was monitored using a microscope (Nikon SMZ 1500) and a DSLR camera (Nikon D7100). *In situ* growth of calcite crystals was initiated after ∼3 hours of the cementation process (Fig. 1). All biogenic calcification was conducted under constant injection rate conditions and flow outlets were open to the atmosphere.

Reactive transport in 2D porous medium micromodel

Pore-scale reactive transport in carbonate medium was visualized using the biogenically calcite-functionalized micromodels. High-temperature, high-pressure experiments corresponding to subsurface conditions (*i.e.*, supercritical CO_2 conditions) were conducted. High-pressure fluid delivery to the micromodel was enabled using an aluminum manifold and nanoports (Upchurch/IDEX). Two high-pressure pumps (Quizix QX) supplied the pressurized acidic injectant fluids at a constant rate and maintained the outlet of the micromodel at a constant pressure (Fig. 2). Specifically, CO_2 was added to an accumulator (Swagelok 304L-HDF4-300) filled with 200 mL of acidic fluid (0.5, 1, and 2 wt% HCl) at 8.27 MPa to ensure that the injection acid was fully saturated with $CO_{2(aq)}$. The acid was equilibrated with pressurized CO_2 overnight to ensure CO_2 saturation in the aqueous phase. Backpressure was maintained at 8.27 MPa with DI water. The pressurized micromodel was submerged in a heated water bath maintained at 35 °C to ensure that the separate CO_2 phase was supercritical to model reservoir conditions. Hot water was circulated to the water bath using an external heated bath (Digital Plus Thermo Scientific NESLAB RTE17). Flow and dissolution dynamics were visualized using a microscope (Nikon SMZ 1500) and a DSLR camera (Nikon D7100).

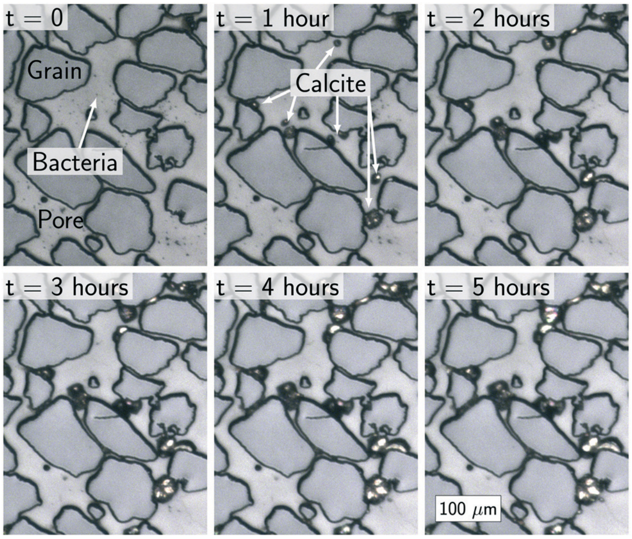

Fig. 1 *In situ* growth of calcium carbonate (calcite) crystals within the micromodel pore space. *Sporosarcina pasteurii* bacteria were deposited into the micromodel and *in situ* microbial growth was encouraged by injection of the brain heart growth medium (t = 0). Calcite precipitation was induced with the injection of the urea/$CaCl_2$ cementation solution ($t \geq 1$ hour). Calcite grains were grown securely on the pore surfaces throughout the micromodel after ∼3 hours. Calcite grains appear white due to their natural refractive tendencies without digital image enhancement.

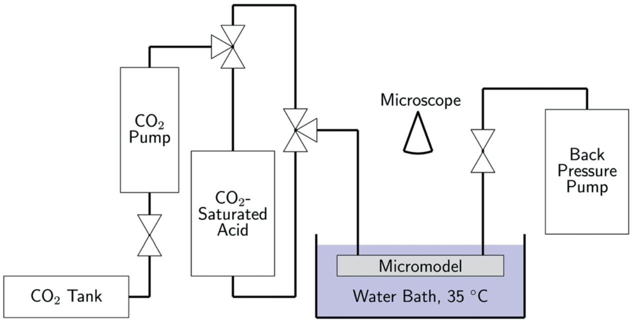

Fig. 2 Experimental setup for high-temperature, high-pressure microvisualization of reactive transport in a 2D calcite micromodel. The micromodel is submerged in a heated water bath and two high-pressure pumps are used to deliver injection fluids and maintain system pressure. The CO_2 pump was used to reach reservoir pressures and deliver the CO_2-saturated acid to the calcite micromodel. The backpressure (BP) pump was filled with DI water to maintain system pressure at 8.27 MPa.

Calcite-embedded polymer microchannel

Single-channel polymer microfluidics facilitated systematic investigation of the parametric influence of injection acid concentration, flow rate, and solubility on reactive transport in carbonate formations. A single octagonal calcite post embedded in a soft, nonreactive PDMS polymer channel enabled controlled experimental parameters, *i.e.*, local advection and reaction rates (Fig. 3(b)). To fabricate the visualization platform, a silicon mold (rectangular ridge 37 mm in length, 1.5 mm in width, and 200 μm in depth) was first created using standard photolithography and deep reactive ion etching techniques (Fig. 3). Non-reactive polymer (10 : 1 PDMS, silicone elastomer, Sylgard) was mixed, degassed, and poured

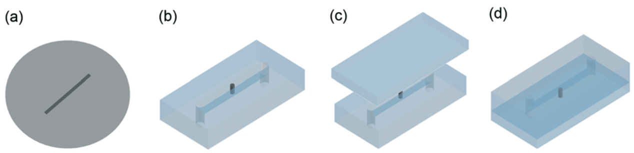

Fig. 3 Fabrication technique for the single-crystal, single-channel polymer microfluidic platform. (a) A single rectangular ridge was molded onto a silicon wafer using standard photolithography and deep reactive ion etching techniques. (b) PDMS was poured onto the silicon mold and under-cured to ensure a secure seal between the embedded calcite crystal and the channel surface. (c) The calcite-embedded open channel was sealed with a second PDMS plate and heated until fully cured and bonded (d). The embedded calcite crystal was 500 μm wide and the channel was 1.5 mm × 200 μm in cross section.

onto the silicon mold to cure and form the chemically inert microchannel. A slight modification of standard PDMS curing procedures (70 minutes at 50 °C) was made such that the PDMS was under-cured to embed the calcite crystal securely. The under-cured PDMS channel was then peeled from the silicon mold and inlet and outlet ports were drilled to allow for flow. The PDMS was then cleaned with soap and DI water and placed on a clean glass plate. Trapped air bubbles between the PDMS and the glass plate lead to optical artefacts that impair visualization, and thus a good seal between the two materials is desired. A single octagonal calcite post (500 μm wide, 300 μm height) was then placed in the center of the channel. Note that the calcite post was taller than the channel walls to ensure that (i) the calcite crystal was firmly embedded in the channel and (ii) the top and bottom surfaces of the octagonal calcite post were firmly sealed to the polymer to minimize any two-dimensional effects. Teflon tweezers were used to avoid damaging the crystal surface because scratches on the calcite surface create additional reaction sites and bubble nucleation sites that reduce the repeatability of the experiments. Lastly, a flat sheet of under-cured PDMS was placed on top of the calcite-embedded open channel and heated on a hot plate at 110 °C for 15 minutes to cure and bond completely.

Reactive transport in 1D polymer microchannel

Reactive transport parameters were studied systematically using the single-grain polymer-based microchannel platforms. Acid concentrations of 0.5, 1, and 2 wt% HCl injected at flow rates of 10, 50, and 100 m per day were tested. All experiments were conducted under ambient conditions and the outlet was open to the atmosphere. The corresponding dimensionless quantities comparing rates of reaction, advection, and diffusion are listed in Table 1. The dimensional experimental parameters, while different from real geological systems, are nondimensionalized to correspond to realistic conditions regardless of scale. Specifically, the Peclet (Pe = advection/diffusion), Damkohler (Da = reaction/advection), and modified Stanton (St = solvation/advection) numbers are extracted from the experiments (see detailed explanations in Results and discussion). Acids were delivered using a syringe pump (Harvard Apparatus, Holliston, MA) and a 10 mL syringe (BD 10 mL syringe, 309604). Reactive transport dynamics were visualized using a microscope and camera setup (Leica Z16 APO).

Table 1 Dimensionless quantities corresponding to the experimental conditions used. The column labeled regime corresponds to the phase map in Fig. 9

Pe	Da	St	PeDa	Regime
1.94	7.52	0.516	14.6	III
10.5	2.51	0.095	26.5	III
10.5	0.677	0.095	7.13	III
2.10	16.6	0.475	34.9	III
124.45	0.0750	2.50	9.33	I
12.45	0.0121	0.00478	0.150	II
62.23	0.0196	0.816	1.22	I
62.23	0.0310	1.08	1.93	I

Results and discussion

New grain-engulfment mechanism during reactive transport

Dynamics at the reactive interface underlies reactive transport and CO_2 storage security fundamentally. Calcite-embedded microchannels were used to visualize directly the interface-scale transport dynamics. Importantly, direct interface-scale observations show a new fundamental mechanism, herein called the grain-engulfment mechanism, whereby the reaction product CO_2 forms a separate, protective phase around the calcite grain that prevents contact between the reactants (*i.e.*, the acid and the dissolving carbonate grain, Fig. 4). Implications of the grain-engulfment effect extend past CO_2 storage and the subsurface; the protective effect is fundamental and of significance to reactive transport through porous medium in general.[28]

Recall that in this setup, a single reactive calcite grain is embedded within a non-reactive PDMS microchannel to control the reaction and advection rates delivered to the reaction interface (Fig. 4a). Dilute hydrochloric acid, a proxy to the CO_2-acidified brine that develops during CO_2 injection in underground aquifers, was injected into the microchannel to induce calcite dissolution. Downstream pressure was maintained at 1 atm. Whereas the pH of CO_2-acidified reservoir brine in geological storage systems is high (pH ∼3.4–4),[53] the low pH here (pH ∼0.26–0.86) provides a method to speed up dissolution kinetics in the laboratory. Despite the low pH and pressures here, we scale our experimental parameters such that they correspond to the dimensionless parameters that represent realistic geological CO_2 storage conditions. Importantly, considering the impurities such as sulfur and nitrogen oxides that are inevitably present in the injected CO_2 stream[36] due to economics, the pH of the reservoir is reduced to pH 1.[54,55] The experimental conditions that we impose are thus representative of industrial-scale geological CO_2 storage conditions.

The grain-engulfment mechanism that is observed here is of fundamental importance to the understanding and the prediction of reactive transport in the subsurface. The grain-engulfment mechanism is characterized by an initial constant rate of reaction (Fig. 4a, t = 0 to t = 393.08 s; Fig. 4b, steady dissolution) followed by a subsequent phase of zero grain dissolution (Fig. 4a, t = 393.40 s onwards; Fig. 4b, grain engulfment) due to the lack of a direct reaction interface (*i.e.*, grain engulfment). Specifically, a separate CO_2 phase was generated and retained at the calcite grain surface (Fig. 4a). The retained separate CO_2 phase prevents reaction between the rock and the acid due to a lack of direct solid/aqueous phase interface (Fig. 4a, t = 37.40 s to t = 695.00 s). The time resolution of the pore-level dynamics here is 0.04 s due to high-resolution video recording capabilities at 25 frames per second.

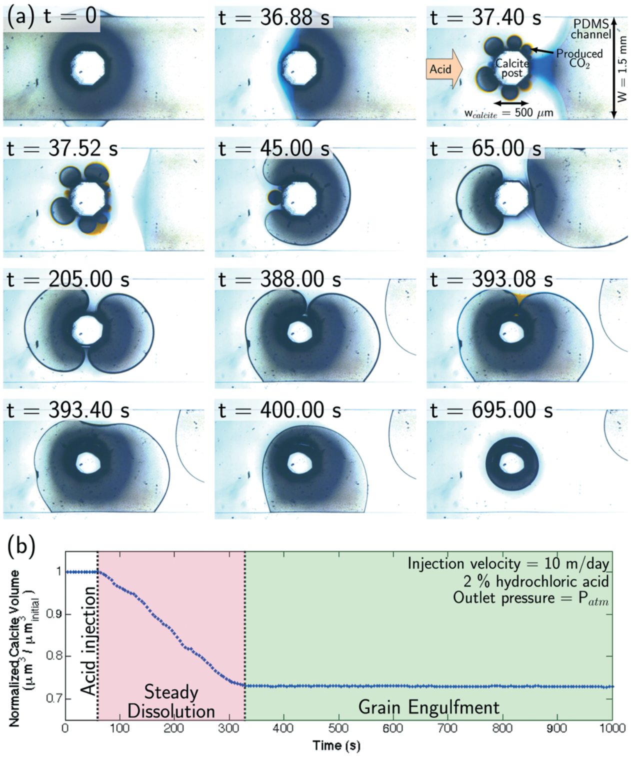

Fig. 4 Grain-engulfment phenomenon in single-grain polymer microchannels. (a) Time evolution of a single grain in an initially air-filled channel (*t* = 0). Acid is introduced (*t* = 36.88 s), and thereafter the reaction with the calcite grain is observed. Specifically, the initial dissolution reaction (*t* = 37.40 s, 37.52 s) is rapid and produces small CO_2 bubbles due to exposed reaction sites introduced through the fabrication process. Expenditure of the active sites and coalescence of small bubbles results in large bubbles (*t* = 45.00 s). Large bubbles are advected downstream due to pressure buildup across its body (*t* = 65.00 s). Continued growth of the CO_2 bubbles around the calcite grain, however, is sustained (*t* = 205.00 s) and its coalescence leads to partial engulfment (*t* = 388.00 s, 393.08 s) that results in asymmetric grain dissolution. Occurrence of the grain-engulfment event (*t* = 393.40 s) due to bubble collapse around the calcite grain isolates the grain from further reaction, and subsequent dissolution is halted (*t* = 400.00 s, *t* = 695.00 s) until the separate CO_2 phase is diffused into the aqueous phase. (b) Calcite grain volume decreases linearly over time prior to complete grain engulfment and remains constant thereafter until all of the engulfing CO_2 is solubilized into the aqueous phase (not shown).

Simple flow geometries sustain bubble retention and growth around the calcite grain and result in complete calcite grain engulfment (Fig. 4a, *t* = 393.40 s). Quantitative analysis from image processing showed constant overall dissolution rates prior to complete engulfment and no dissolution afterwards (Fig. 4b). Calcite grain dissolution resumed once the engulfing separate CO_2 phase was completely solubilized into the aqueous phase and fresh reaction interfaces were exposed; the grain engulfment/CO_2 solvation cycle continued until all of the local calcite dissolved. This stepwise dissolution phenomenon due to separate CO_2 phase grain engulfment delays local dissolution and preserves the acid for downstream reactions. Prior to full grain engulfment, partial grain envelopment did not drastically alter the rate of overall grain dissolution. Local dissolution, however, was halted in regions occupied by the CO_2 phase due to the lack of a direct reaction interface and was expedited in regions where grains were exposed to acidic solution. Reactive transport around semi-engulfed grains thereby resulted in asymmetric grain dissolution. We interpret this as characteristic of a transport-limited process.

The importance of the separate CO_2 phase on reactive transport is explained by comparing dominant forces about evolved CO_2 bubbles. For typical subsurface flows, the retaining surface tension force, $F_{\mathrm{IFT}} = \gamma 2\pi r \cos\theta \sim O(10^{-8}\ \mathrm{N})$, is approximately three orders of magnitude greater than the inertial viscous drag force, $F_{\mathrm{d}} = 6\pi\mu R u \sim O(10^{-11}\ \mathrm{N})$. We use values for interfacial tension $\gamma \sim 34\ \mathrm{mN\ m^{-1}}$,[56] bubble radius $r \sim 1\ \mu\mathrm{m}$ corresponding to typical bubble size measured from the experiments, viscosity $\mu \sim 0.7$ mPa s, and a pore velocity $\mu \sim 1$ to 50 m per day, typical of subsurface flows. Contact angle contributions ($\cos\theta$) to the retaining force are order one and therefore have little influence on the mobility of the CO_2 bubble away from the reaction interface. Dominance of surface tension, importantly, retains the separate CO_2 phase in the pore space and enables grain engulfment.

Significance of separate CO_2 phase at pore and ensemble scales

The grain-engulfment effect holds in porous configurations regardless of pressure so long as a separate CO_2 phase is present. Grain-engulfment implications at pore and pore-network-ensemble scale on reactive transport through porous media were investigated using the chemically and geometrically representative biogenically calcite-functionalized micromodels developed in this work. SEM-energy dispersive X-ray spectroscopy (EDS) and X-ray crystallography (XRD) characterization of the calcite grains resulting from biogenic functionalization shows comparable composition and crystallography, respectively, to natural calcite crystals.[49,51,52] The ensemble scale is defined here to be a set of pores on the order of the representative elementary volume of the porous medium. In the following, pressures and temperatures corresponding to gaseous and supercritical CO_2 were imposed to investigate grain engulfment and separate CO_2 phase evolution at the pore and ensemble scales under ambient (Fig. 5) and reservoir conditions close to (Fig. 7) and far from (Fig. 6) the well.

We find that gas-phase CO_2 evolves rapidly at low-pressures (Fig. 5) and supercritical-phase CO_2 develops at later times at storage reservoir pressures (Fig. 7) due to increased CO_2 solubility in water. Under reservoir conditions, ensemble-scale dissolution rates remain constant and pore-scale dissolution is dictated by grain engulfment (Fig. 7), consistent with low-pressure observations. Specifically, exposed grains dissolve at a constant rate, whereas engulfed grains experience no dissolution (Fig. 7); hence, capillary trapping of the separate CO_2 phase determines the spatial allocation of

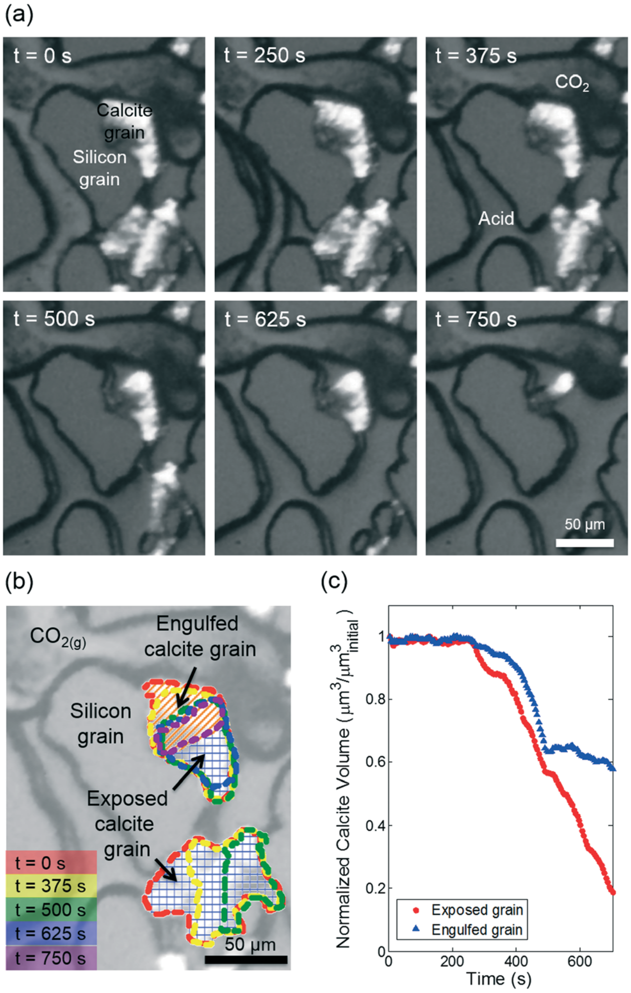

Fig. 5 Grain engulfment due to separate CO_2-phase formation in a calcite–silicon micromodel. (a) Grain engulfment dominates the top calcite grain that is shielded by the separate CO_2 phase and rapid dissolution rates dictate dissolution of the bottom acid-exposed calcite grain. (b) Time-evolution of calcite grain boundaries. Regions protected by CO_2 (diagonally hatched) experience little dissolution and regions exposed to acid (square-hatched) dissolve rapidly. (c) Size of exposed (red) and engulfed (blue) calcite grains shows a rapid, constant rate of carbonate dissolution for single-phase regions and minimal dissolution for CO_2-wetted surfaces.

grain dissolution in porous media. Pore-body grain dissolution dominates over pore-throat grain dissolution (Fig. 7) due to exposure to the non-wetting acid phase in pore bodies and the CO_2 phase residence in pore throats. Pore- and ensemble-scale grain engulfment therefore dictates reactive transport through porous media under atmospheric and subsurface reservoir conditions due to separate CO_2 phase formation.

Pore-scale grain-engulfment under ambient conditions

Similar to the single-grain micro-channel study, micromodel experiments show that grain-engulfment dictates the structural deterioration of the calcite porous medium due to CO_2 phase evolution. Separate CO_2 phase produced and retained on calcite surfaces (Fig. 5a and b) insulated calcite grains from acidic constituents and thereby inhibited local dissolution. Following separate CO_2 phase evolution in the pore space, grains exposed to acid continued to dissolve rapidly (Fig. 5b, square-hatched region, and c), whereas grains bounded by CO_2-wetted surfaces did not dissolve at all (Fig. 5b, diagonal-hatched region, and c).

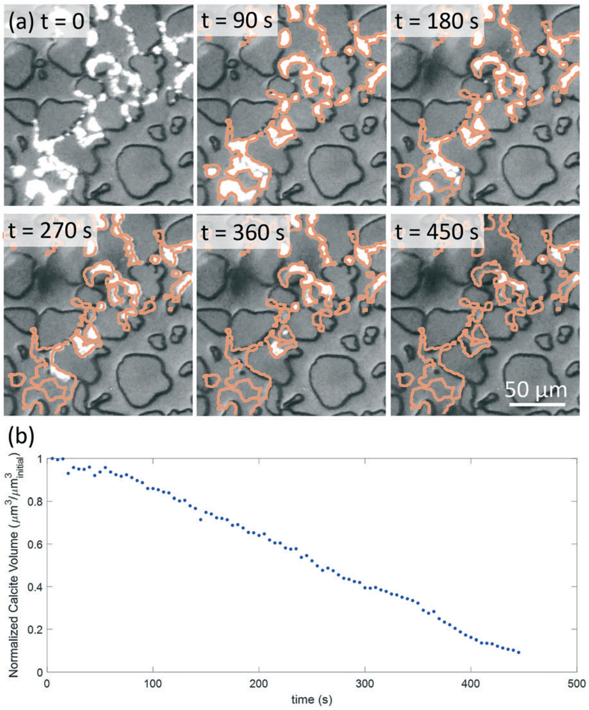

Fig. 6 Extent of the grain-engulfment effect is minimized under conditions of slow reaction rate relative to solubilization of CO_2 in the aqueous phase. (a) A separate, protective CO_2 phase is not developed due to high solubility of CO_2 in the aqueous phase at elevated pressures. Calcite dissolution (original grain outlines are traced for comparison) is rapid. (b) Calcite was dissolved at a constant and rapid rate due to the lack of a separate, protective CO_2 phase.

Interestingly, an episodic CO_2 bubble-induced flow distortion mechanism was observed that dissolved CO_2-engulfed calcite grains adjacent to water-wet surfaces. Specifically, continuous aqueous phase flow is initially distorted by reaction-induced CO_2 bubble formation. The nucleated bubble is initially immobile because the differential pressure drop across its short length is insufficient to overcome capillary forces. Upon growth to its critical mobilization length, the bubble advects downstream and aqueous acid refills the pore space. Pore pressure-instabilities in the continuous acid phase disperse protective CO_2 bubbles away from water-wet silicon surfaces momentarily and introduce acid to the previously protected calcite surface. Protective CO_2 bubbles resume their original configuration following pore-pressure re-equilibration and thus create small acid pockets for reaction. Calcite grains adjacent to acid pockets dissolve locally until complete acid consumption is achieved. Our porous media experiments show that grain engulfment reduces the local rate of calcite dissolution and prolongs the spatial distribution of acidic constituents through flow diversion.

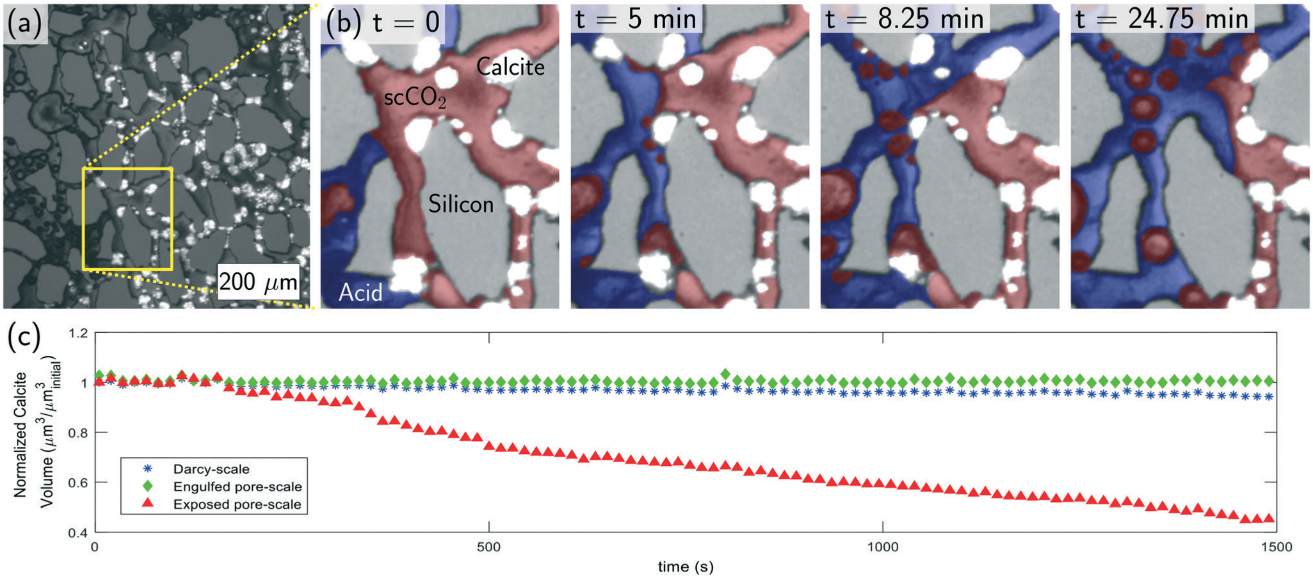

Fig. 7 Grain engulfment dictating calcite dissolution at pore and pore-ensemble scales close to the well under geological conditions. (a) Ensemble-scale carbonate dissolution and separate supercritical CO_2 phase formation under storage reservoir conditions. CO_2-saturated 2 wt% HCl acid is injected at 5 m per day, 8.27 MPa, and 35 °C and long dissolution paths (*i.e.*, wormholes) are observed macroscopically. (b) Pore-level calcite grain engulfment due to separate $scCO_2$ phase. Pore-throat grains engulfed by the separate CO_2 phase are isolated from acid and experience no dissolution, whereas exposed pore-body grains dissolve rapidly. Initially at *t* = 0, the pore displayed is saturated with $scCO_2$ and CO_2-saturated acid is injected from left to right. Pressure fluctuations with flow induce CO_2 bubble snap-off in the small, water-wet pores and expose the calcite grain to acid (*t* = 5 min). $scCO_2$ bubbles are produced and wet the grain, leading to grain engulfment (*t* = 5 min, *t* = 8.25 min). Local rates of dissolution are retarded due to calcite grain engulfment by the $scCO_2$ (*t* = 24.75 min). (c) Comparison of ensemble- and pore-scale calcite dissolution. Ensemble-scale calcite dissolution occurs at a constant rate, whereas pore-scale dissolution is dictated by local conditions (exposed *vs.* engulfed).

Pore-scale grain engulfment under reservoir conditions

Subsurface systems are characterized by elevated temperatures and elevated pressures (*e.g.*, $P \gtrsim 1000$ psi). Two important fluid properties impact the significance of the grain-engulfment effect under extreme reservoir conditions. First, CO_2 enters its supercritical phase at high temperature and pressure conditions. Supercritical CO_2 density (567 kg m^{-3} at 35 °C and 1200 psi) is much higher than gaseous CO_2 density at ambient conditions (1.8 kg m^{-3} at 25° and 14.7 psi). Increased separate CO_2 phase density reduces the local CO_2 volume fraction, *i.e.*, saturation, as CO_2 is produced due to calcite grain dissolution. Recall that the local saturation of the separate CO_2 phase determines the extent to which the grain surfaces are protected from the encroaching acidic brine.

Second, the solubility of CO_2 in the aqueous phase varies with pressure and temperature. Importantly, CO_2 solubility increases drastically with increasing pressure and decreases with temperature. The solubility of CO_2 in the aqueous phase determines the formation of a separate CO_2 phase: increased separate CO_2 phase formation is due to decreased solubility, whereas increased solubility results in decreased formation of a separate, protective CO_2 phase. In this study, we focus on elevated pressure systems due to its minimizing impact on the grain-engulfment effect in reservoirs.

Pore-scale grain engulfment under reservoir conditions of slow reaction relative to CO_2 solvation

Far away from the well, reservoir fluids are unaltered and in their initial geological state (*i.e.*, not perturbed and/or saturated with CO_2). The capacity for CO_2 solvation into the aqueous phase is, as a result, large. Injection of 2 wt% HCl that is not saturated with CO_2 into the pore space shows rapid dissolution of the carbonate matrix without production of a separate, protective CO_2 phase (Fig. 6).

Pore-scale grain engulfment under reservoir conditions of fast reaction relative to CO_2 solvation

In the vicinity of the CO_2 front, reservoir brine is displaced by and in contact with the injected CO_2. Local exposure and mixing enables equilibration between CO_2 and the aqueous brine, and, as a result, for CO_2 to saturate the aqueous phase. Under pre-equilibrated situations where the aqueous phase is saturated with CO_2, additional CO_2 that is released due to the calcite dissolution reaction is forced to develop into a separate, protective phase, as was observed under ambient conditions. Specifically, we inject CO_2-saturated acid and impose pressures (1200 psi) and temperatures (35 °C) that correspond to supercritical CO_2 to investigate grain engulfment and separate CO_2 phase evolution at reservoir locations close to the well. We find that a separate, protective supercritical CO_2 phase develops at storage reservoir pressures (Fig. 7), similar to the gas-phase CO_2 that evolved rapidly at low pressures (Fig. 5).

Under near-wellbore reservoir conditions, ensemble-scale dissolution rates remain constant and pore-scale dissolution is dictated by grain engulfment (Fig. 7), consistent with low-pressure observations. Specifically, exposed grains dissolve at a constant rate, whereas engulfed grains experience no dissolution (Fig. 7); hence, capillary trapping of the separate CO_2 phase determines the spatial allocation of grain dissolution in porous media. Interestingly, pore-body grain dissolution dominates over pore-throat grain dissolution (Fig. 7) due to exposure to the non-wetting acid phase in pore bodies and the separate CO_2 phase residence in pore throats. An approximately constant rate of dissolution is observed at the Darcy scale as a result of the combined effects in protected and exposed pores. The total rate, while constant (~5% total dissolution over 1500 s at the Darcy scale in Fig. 7c, blue), is less than would be expected if the system had remained single phase (~95% total dissolution over 450 s at the Darcy scale in Fig. 6). Pore-scale effects that determine dissolution patterns, however, are masked. Pore- and ensemble-scale grain engulfment therefore dictates reactive transport through porous media under atmospheric and subsurface reservoir conditions due to separate CO_2 phase formation.

The grain-engulfment mechanism

Grain engulfment underlies dissolution in pores and pore ensembles (Fig. 8), much like in the hydrodynamically simple 1D geometry (Fig. 4). At the ensemble scale, acidic fluid bypasses the CO_2-protected calcite grains and instead diverts to fresh, water-saturated calcite pores downstream that are susceptible to direct reaction (Fig. 8). Preferential flow paths were observed that span the entire micromodel. This is a macroscopic observation collected by imaging the whole micromodel (*i.e.*, not pore scale). Grain engulfment restricts preferential flow path enlargement in the direction normal to flow and the resulting acid flow diversion promotes lengthwise preferential flow path extension. These model-scale observations are in consensus with core-scale experiments.[57] On the ensemble scale, grain engulfment protects initial conduits from further dissolution and leads to long and narrow preferential flow path development.

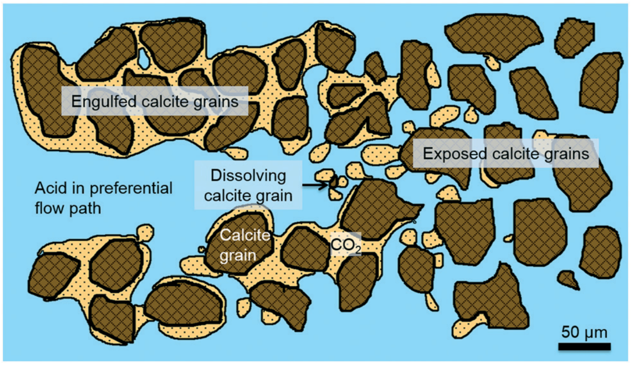

Fig. 8 Ensemble-scale preferential flow path propagation due to separate CO_2 phase grain engulfment and acid diversion.

Phase map of reactive transport and of grain engulfment

The results of this study provide direct observations at the interface, pore, and pore-ensemble scales to delineate the underlying grain-engulfment mechanism in reactive transport through carbonate systems. Importantly, we uncover the interplay between transport, reaction, and phase evolution during the dissolution of a reactive porous matrix through experiments under conditions corresponding to ambient, near-well, and far-from-well locations. Geological CO_2 storage security implications due to the grain-engulfment mechanism requires upscaled understanding of reactive transport in storage formations. Dimensionless quantities enable upscaling from the pore-scale, laboratory conditions to reservoir scales and conditions.

Scaling parameters of transport, reaction, and CO_2 solvation into the aqueous phase were mapped systematically using the calcite-embedded polymer microchannel (see Table 1 for experimental conditions). The rates of advection are determined by the injection rate and cross-section geometry of the polymer channel. Rates of reaction, diffusion, and solvation are determined through analysis of visual image data. The simple geometry here provides a means of systematic study while eliminating extraneous complexities associated with the hydrodynamics of porous media. Direct interface-scale observations show three distinct carbonate dissolution regimes (Fig. 9): constant slow dissolution with CO_2 dissolved in the aqueous phase at small acid fluxes (regime I), separate CO_2 phase generation under intermediate conditions (regime II), and stepwise, rapid dissolution with separate CO_2 phase grain- engulfment at large acid fluxes (regime III).

In regime I (see also Fig. 6), a small acid flux to the reaction interface results in slow rock dissolution and hence slow CO_2 generation. CO_2 solubility under these conditions exceeds the rate of CO_2 generation and rate of CO_2 advection away from the interface, resulting in immediate CO_2 solvation into the aqueous phase. No separate CO_2 phase was observed as a result. Grain dissolution rates observed in regime I are determined by acid flux to the reaction interface, in agreement with the single-phase reactive transport theory. This regime corresponds to the far-from-well reservoir condition study in the calcite-functionalized micromodel.

Regimes II and III (see also Fig. 4, 5, and 7), by contrast, are characterized by rates of reactive CO_2 generation that far exceed the rate of CO_2 solvation into the aqueous phase and rate of CO_2 advection away from the reaction interface. Importantly, under these conditions, a separate CO_2 phase evolves. Regime II is distinguished by transport rates that exceed the rate at which CO_2 is produced from the reaction. This reaction-limited process generated separate CO_2 phase slowly. Constant calcite dissolution rates were observed in regime II, similar to regime I.

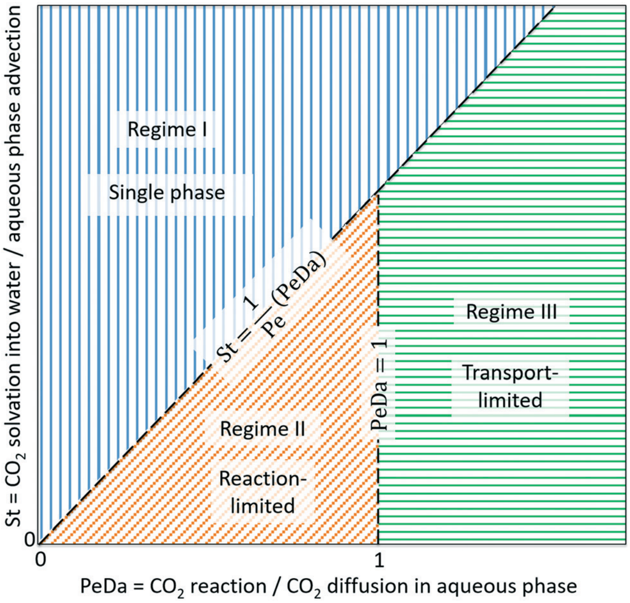

Fig. 9 Phase map of grain-engulfment regimes. The grain-engulfment effect is significant in regime III (green horizontal hatching) where reactive CO_2 production rates exceed solvation rates of CO_2 into the aqueous phase (St < Da) and where transport-limited conditions dominate (PeDa > 1). At the Darcy scale, wormholing occurs in regime III where the dissolution process is transport limited. Wormholing is a macroscopic observation. The reaction product CO_2 is diffused into the aqueous phase directly in regime I (blue vertical hatching). A separate CO_2 phase also forms in regime II (orange diagonal hatching). Reaction-limited conditions encourage relatively uniform growth of the CO_2 phase.

Regime III, however, is transport-limited and is governed by grain engulfment. We describe the separate CO_2 phase evolution using (i) the Peclet–Damkohler number (PeDa) to compare the rate of CO_2 generation due to reaction with the rate of CO_2 diffusion in the aqueous phase, and (ii) the modified Stanton number (St) to compare the rate of CO_2 solvation into the aqueous phase to the rate of aqueous phase advection. We determine the necessary conditions for separate, protective CO_2 phase evolution as (i) $St < Da$ in order to achieve a separate CO_2 phase (*i.e.*, rate of CO_2 solvation into the aqueous phase is less than the rate of CO_2 production due to reaction), and (ii) $PeDa > 1$ in order to achieve transport-limited conditions[21] to retain the separate CO_2 phase around the calcite grain (Fig. 5). The pore-scale studies under near-well reservoir conditions reside in regime III.

While it is true that full physics simulation of reactive transport is required to predict the security of a given geological CO_2 storage site, consideration of the local conditions delineated by the phase diagram (Fig. 9) provides a first-order understanding of the storage system. Here we demonstrate using direct, experimental observation and dimensionless scaling that the grain-engulfment effect is expected to extend into the reservoir. Specifically, the regimes delineated through experiments at the interface scale (Fig. 8) are applicable at reservoir conditions by mapping the dimensionless quantities Pe, Da, and St using pore-scale values of interstitial velocity, $V_{\text{pore}} = f(\phi, S)$, corrected for mutliphase flow from large-scale (*i.e.*, Darcy- and reservoir-scale) systems (*e.g.*, porosity, ϕ, and saturation, S). Previous visualization in three-dimensional core samples provides more realistic geometric perspectives but is limited by spatiotemporal resolution. The question of additional geometric dimensions is addressed here through the upscaling from a 1D microchannel to a 2D porous network. Specifically, care was taken to increase the pore connectivity of the 2D micromodel such that it is representative of a 3D core sample without forfeiting real-time pore-level visualization capability.[34,37]

Conclusions

We develop a novel biogenic-calcite-functionalized mirovisualization device to delineate the fundamental dynamics dictating reactive flows through geologic carbonate formations. Using the novel device, we discover a new mechanism, grain engulfment, that underlies the complex rock dissolution dynamics in reactive carbonate formations and offers fundamental understanding to develop predictive models for subsurface CO_2 storage assessment. We find that carbonate dissolution under typical reservoir conditions results in a separate CO_2 phase that impedes local dissolution and promotes downstream reactions. Our experimental results and theoretical framework show that separate CO_2 phase-induced grain engulfment is an important mechanism in determining the overall storage and security of geologic storage reservoirs. When combined with advanced simulation and geological data, our results have the potential to provide an accurate predictive model to assess subsurface CO_2 storage security in carbonate formations.

Conflicts of interest

There are no conflicts to declare.

Acknowledgements

The authors gratefully acknowledge funding from Chevron ETC, the Hormoz and Fariba Ameri Graduate Education Fellowship in Earth Sciences, and the Petroleum Research School of Norway STEP scholarship. The authors gratefully thank Professor Hamdi Tchelepi for discussions on the experiments and the manuscript. The authors also gratefully acknowledge discussions with James Minto from the University of Strathclyde on biogenic calcite precipitation and assistance in developing the bacterial growth protocol from Debra Hausladen and Professor Scott Fendorf at Stanford University. In addition, the authors gratefully thank Dr. Steinar Sørnes at the University of Bergen for helping to grow the bacteria. The authors also acknowledge Dr. Cynthia M. Ross for her contribution in creating the original silicon micromodel geometry and Dr. Sophie Roman for discussions on image processing techniques, both from Stanford University.

Notes and references

1 A. Kovscek and Y. Wang, *Energy Convers. Manage.*, 2005, **46**, 1920–1940.

2 S. Pacala and R. Socolow, *Science*, 2004, **305**, 968–973.

3 S. Solomon, D. Qin, M. Manning, Z. Chen, M. Marquis, K. Averyt, M. Tignor and H. Miller, *Contribution of Working Group I to the Fourth Assessment Report of the Intergovernmental Panel on Climate Change, 2007*, Cambridge University Press, 2007, vol. 53.

4 E. Dlugokencky and P. Tans, *Trends in Atmospheric Carbon Dioxide*, 2016.

5 A. Kovscek and M. Cakici, *Energy Convers. Manage.*, 2005, **46**, 1941–1956.

6 M. D. Zoback and S. M. Gorelick, *Proc. Natl. Acad. Sci. U. S. A.*, 2012, **109**, 10164–10168.

7 K. Z. House, D. P. Schrag, C. F. Harvey and K. S. Lackner, *Proc. Natl. Acad. Sci. U. S. A.*, 2006, **103**, 12291–12295.

8 J. M. Matter and P. B. Kelemen, *Nat. Geosci.*, 2009, **2**, 837–841.

9 S. Whittaker, *IEA GHG Weyburn CO 2 Monitoring & Storage Project*, 2004, Ieaghg technical report.

10 F. M. Orr, *Science*, 2009, **325**, 1656–1658.

11 J. Dooley, R. Dahowski, C. Davidson, M. Wise, N. Cupta, S. Kim and E. Malone, *Carbon Dioxide Capture and Geologic Storage - A Core Element of Global Energy Technology Strategy to Address Climate Change*, 2006, Epa technical report.

12 M. A. Celia, S. Bachu, J. M. Nordbotten and K. W. Bandilla, *Water Resour. Res.*, 2015, **51**, 6846–6892.

13 W. Song, T. W. de Haas, H. Fadaei and D. Sinton, *Lab Chip*, 2014, **14**, 4382–4390.

14 X. Fu, L. Cueto-Felgueroso, D. Bolster and R. Juanes, *J. Fluid Mech.*, 2015, **764**, 296–315.

15 M. J. Bickle, *Nat. Geosci.*, 2009, **2**, 815–819.

16 T. A. Buscheck, J. A. White, S. A. Carroll, J. M. Bielicki and R. D. Aines, *Energy Environ. Sci.*, 2016, **9**, 1504–1512.

17 E. Bemer and J. Lombard, *Oil Gas Sci. Technol.*, 2010, **65**, 445–459.

18 D. J. Garcia, H. Shao, Y. Hu, J. R. Ray and Y.-s. Jun, *Energy Environ. Sci.*, 2012, 5758–5767.

19 M. Fleury, J. Pironon, Y. M. Le Nindre, O. Bildstein, P. Berne, V. Lagneau, D. Broseta, T. Pichery, S. Fillacier, M. Lescanne and O. Vidal, *Energy Procedia*, 2011, **4**, 5227–5234.

20 B. K. Brunk, G. H. Jirka and L. W. Lion, *Environ. Sci. Technol.*, 1997, **31**, 119–125.

21 H. Ott and S. Oedai, *Geophys. Res. Lett.*, 2015, **42**(7), 2270–2276.

22 P. Nguyen, H. Fadaei and D. Sinton, *J. Fluids Eng.*, 2013, **135**, 021203.

23 C. N. Fredd and H. S. Fogler, *AIChE J.*, 1998, **44**, 1933–1949.

24 C. N. Fredd and H. S. Fogler, *SPE J.*, 1998, 34–41.

25 M. L. Hoefner and H. S. Fogler, *AIChE J.*, 1988, **34**, 45–54.

26 K. Lund, H. S. Fogler, C. McCune and J. Ault, *Chem. Eng. Sci.*, 1975, **30**, 825–835.

27 Y. Yang, C. Ronziob and Y.-S. Jun, *Energy Environ. Sci.*, 2011, 4596–4606.

28 S. K. Reinke, S. V. Roth, G. Santoro, J. Vieira, S. Heinrich and S. Palzer, *ACS Appl. Mater. Interfaces*, 2015, **18**, 9929–9936.

29 R. S. Middleton, G. N. Keating, P. H. Stauffer, A. B. Jordan, H. S. Viswanathan, Q. J. Kang, J. W. Carey, M. L. Mulkey, E. J. Sullivan, S. P. Chu, R. Esposito and T. A. Meckel, *Energy Environ. Sci.*, 2012, **5**, 7328–7345.

30 Y. Kim, J. Wan, T. J. Kneafsey and T. K. Tokunaga, *Environ. Sci. Technol.*, 2012, **46**, 4228–4235.

31 T. K. Tokunaga, J. Wan, J. W. Jung, T. W. Kim, Y. Kim and W. Dong, *Water Resour. Res.*, 2013, **49**, 4566–4579.

32 D. Sinton, *Lab Chip*, 2014, **14**, 3127–3134.

33 M. Buchgraber, A. R. Kovscek and L. M. Castanier, *Transp. Porous Media*, 2012, **95**, 647–668.

34 M. Buchgraber, M. Al-Dossary, C. Ross and A. R. Kovscek, *J. Pet. Sci. Eng.*, 2012, **86–87**, 27–38.

35 M. Buchgraber, T. Clemens, L. Castanier and A. Kovscek, *SPE J.*, 2011, **14**, 269–280.

36 W. Song, H. Fadaei and D. Sinton, *Environ. Sci. Technol.*, 2014, **48**, 3567–3574.

37 W. Song and A. R. Kovscek, *Lab Chip*, 2015, **15**, 3314–3325.

38 W. Song and A. R. Kovscek, *J. Nat. Gas Sci. Eng.*, 2016, **34**, 1276–1283.

39 T. W. de Haas, H. Fadaei, U. Guerrero and D. Sinton, *Lab Chip*, 2013, **13**, 3832–3839.

40 A. Sell, H. Fadaei, M. Kim and D. Sinton, *Environ. Sci. Technol.*, 2013, **47**, 71–78.

41 M. Kim, A. Sell and D. Sinton, *Lab Chip*, 2013, **13**, 2421–2662.

42 A. L. Harrison, G. M. Dipple, W. Song, I. M. Power, K. U. Mayer, A. Beinlich and D. Sinton, *Chem. Geol.*, 2017, **463**, 1–11.

43 J. Wan, T. K. Tokunaga, C.-F. Tsang and G. S. Bodvarsso, *Water Resour. Res.*, 1996, **32**, 1955–1964.

44 L. P. Hauge, J. Gauteplass, M. D. Høyland, G. Ersland, A. Kovscek and M. A. Fernø, *Int. J. Greenhouse Gas Control*, 2016, **53**, 178–186.

45 S. Almenningen, J. Flatlandsmo, A. R. Kovscek, G. Ersland and M. A. Fernø, *Lab Chip*, 2017, **17**, 4070–4076.

46 M. L. Porter, J. Jiménez-Martínez, R. Martinez, Q. McCulloch, J. W. Carey and H. S. Viswanathan, *Lab Chip*, 2015, **15**, 4044–4053.

47 M. Buchgraber, *PhD thesis*, Stanford University, 2013.

48 G. E. Mountassir, R. J. Lunn, H. Moir and E. Maclachlan, *Water Resour. Res.*, 2014, **50**, 1–16.

49 E. G. Lauchnor, L. N. Schultz, S. Bugni, A. C. Mitchell, A. B. Cunningham and R. Gerlach, *Environ. Sci. Technol.*, 2013, **47**, 1557–1564.

50 E. G. Lauchnor, D. M. Topp, A. E. Parker and R. Gerlach, *J. Appl. Microbiol.*, 2015, **118**, 1321–1332.

51 A. Vahabi, A. A. Ramezanianpour, H. Sharafi, H. S. Zahiri, H. Vali and K. A. Noghabi, *J. Basic Microbiol.*, 2015, **55**, 105–111.

52 S. Yoosathaporn, P. Tiangburanatham, S. Bovonsombut, A. Chaipanich and W. Pathom-aree, *Microbiol. Res.*, 2016, **186–187**, 132–138.

53 J. E. Elkhoury, P. Ameli and R. L. Detwiler, *Int. J. Greenhouse Gas Control*, 2013, **16**, S203–S215.

54 K. G. Knauss, J. W. Johnson and C. I. Steefel, *Chem. Geol.*, 2005, **217**, 339–350.

55 S. M. Benson and D. R. Cole, *Elements*, 2008, **4**, 325–331.

56 P. Chiquet, J.-L. Daridon, D. Broseta and S. Thibeau, *Energy Convers. Manage.*, 2007, **48**, 736–744.

57 S. Békri, J. Thovert and P. Adler, *Chem. Eng. Sci.*, 1995, **50**, 2765–2791.